

A modular quantum computer based on a quantum state router

Chao Zhou^{1†}, Pinlei Lu^{1†}, Matthieu Praquin², Tzu-Chiao Chien¹, Ryan Kaufman¹, Xi Cao¹, Mingkang Xia¹, Roger Mong¹, Wolfgang Pfaff³, David Pekker¹, Michael Hatridge¹

¹*Department of Physics and Astronomy, University of Pittsburgh, Pittsburgh, PA, USA*

²*Département de Physique, École Normale Supérieure, Paris, France*

³*Department of Physics, University of Illinois Urbana-Champaign, Champaign, IL, USA*

[†]*These authors contributed equally to this publication.*

(Dated: June 5, 2022)

In this work, we present the design of a superconducting, microwave quantum state router which can realize all-to-all couplings among four quantum modules. Each module consists of a single transmon, readout mode, and communication mode coupled to the router. The router design centers on a parametrically driven, Josephson-junction based three-wave mixing element which generates photon exchange among the modules' communication modes. We first demonstrate SWAP operations among the four communication modes, with an average full-SWAP time of 760 ns and average inter-module gate fidelity of 0.97, limited by our modes' coherences. We also demonstrate photon transfer and pairwise entanglement between the modules' qubits, and parallel operation of simultaneous SWAP gates across the router. These results can readily be extended to faster and higher fidelity router operations, as well as scaled to support larger networks of quantum modules.

I. INTRODUCTION

Modular quantum systems offer a very promising route to large scale quantum computers, allowing us to sidestep the requirement for immensely complex, monolithic quantum processors, and instead operate using smaller, simpler quantum modules linked via quantum communication channels^{1–4}.

For atomic scale qubits communicating using optical-frequency states, it is infeasible to couple photons into a communication channel with very high efficiency. This loss of information precludes light from simply being transferred from module to module, instead one must herald instances in which transmission is successful^{5–9}. However, once light has been coupled into a optical fiber, it can be readily distributed over kilometer and longer distances, which readily supports long-range entangled state generation and distributed quantum computation^{10,11}. In superconducting circuits, there have also been several recent demonstrations of similar measurement-based protocols^{12–15}.

However, superconducting circuits can also transfer states directly. For this form of direct state exchange we require strong, switchable couplings from module to the communication channel to enable rapid operations, low losses in the channel, and a dense, reconfigurable network of couplings among many modules^{16,17}. Realizations to date have focused on pairs of quantum modules, with transmission-line based ‘quantum bus’ communication channels and controllable module-bus couplings based on the nonlinearity of Josephson junctions^{18–24}.

In this article, we propose a new scheme for creating a modular superconducting network, which instead creates a nonlinear ‘quantum state router’ with fixed, dispersive couplings to individual quantum modules. The strong, parametrically driven nonlinearity of the quantum state router allows us to only virtually occupy its modes, and thus achieve efficient operations over the router with only

modest requirements for router quality. There is no use of measurement in the router system, operations over the bus can be thought of as direct, parametrically actuated gates between quantum modules. The state router naturally supports all-to-all coupling among several quantum modules, and is naturally extensible to a larger modular network. We have realized the quantum state router using a Superconducting Nonlinear Asymmetric Inductive eLement (SNAIL)-based nonlinearity²⁵, and used it to operate a four module quantum processor.

II. THEORY OF ROUTER OPERATION

The basic structure of our modular quantum computer consists of two major parts: a quantum state router and multiple modules, as shown in Figure 1. Each module consists of a variable number of qubits (one in our present experiment) which have controllable local coupling with each other. In each module there should also be at least one ‘communication’ mode which couples to both the qubits in the module and the quantum state router. This communication mode can either be a qubit, or, as in our work, a long-lived harmonic oscillator which can store information for exchange over the router.

We have realized our modular quantum computer as a 3D superconducting circuit, and have adopted several design rules to guide our efforts. First, the communication modes we use are superconducting 3D cavities, rather than qubits, as they accommodate multiple qubit encoding schemes, including both the Fock encoding we use in this work as well as cat states²⁶, binomial encodings²⁷, GKP-encodings²⁸, etc. This allows our router to be compatible with a wide array of future module designs. Secondly, we emphasize the “modularity” of our system in the additional sense that each module and the router itself exist as independent units which can operate individually, instead of the whole system forming a monolithic

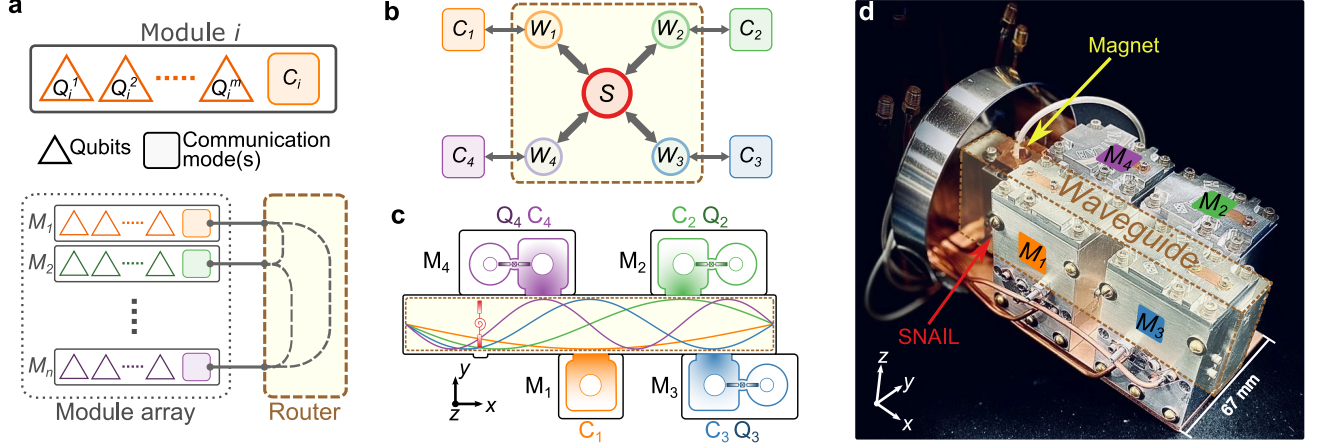


Figure 1. **Schematic representation and picture of the modular quantum computer device** (a) Basic structure of our modular quantum computer, in which a number of quantum modules are connected via their communication modes to a quantum state router. (b) Coupling scheme between the router and four communication modes. The brown dashed square represent the router with four waveguide modes ($W_1 - W_4$) and a SNAIL (S). Each waveguide mode is dispersively coupled to a single communication cavity mode ($C_1 - C_4$). (c) Schematic drawing of the full system consisting four modules and the central quantum state router. The colored curves inside the router represent the E field distribution of the first four waveguide TE_{10n} ($n = 1, 2, 3, 4$) eigenmodes. The SNAIL chip (represented in red) is placed at a location where it couples to all the waveguide modes being used. Each module (for M_2 to M_4) consists of a qubit ($Q_2 - Q_4$), a communication cavity ($C_2 - C_4$) and a readout cavity (for module M_1 the qubit has been omitted). (d) Photograph of the assembled device.

block. This offers a tremendous advantage in the laboratory, as defective components can be easily replaced, and the different components can be tested separately and then assembled. Thirdly, the router operates with SWAP gates based on parametric driving of a 3-wave-mixing Hamiltonian, in which the third order non-linearity is introduced by a SNAIL device. Finally, we have designed the router to minimize both the need for precise frequency matching between router and module modes, and also minimize the requirements for high Q router elements. To accomplish this, we couple all modes in the computer dispersively.

The only nonlinear element is a central SNAIL-mode S (with corresponding annihilation operator \hat{s}), which is very strongly coupled to an input line for strong parametric driving, and flux biased via a nearby copper-sheathed electromagnet. As such, it has a low quality factor Q ($\sim 10,000$). The remainder of the router is composed of a rectangular, superconducting 3D waveguide. The first four transverse electric modes (TE_{10i} , $i = 1, 2, 3, 4$) of the waveguide W_i (with operators \hat{w}_i) are each used as an intermediate mode coupling to both the SNAIL and a corresponding communication mode C_i (with operator \hat{c}_i in the i -th module). The SNAIL is flux biased to a point where its even order non-linear terms are negligible^{25,29} while the third order term is strong, resulting in the Hamiltonian of the router, which has been divided into mode energies, interactions, and nonlinear terms, respectively:

$$\begin{aligned} \hat{\mathcal{H}}_R/\hbar &= \hat{\mathcal{H}}_{R,0}/\hbar + \hat{\mathcal{H}}_{R,int}/\hbar + \hat{\mathcal{H}}_{R,nl}/\hbar \\ &= \left[\omega_s \hat{s}^\dagger \hat{s} + \sum_i \omega_{w_i} \hat{w}_i^\dagger \hat{w}_i \right] + \left[\sum_i g_{w_i s} (\hat{w}_i^\dagger \hat{s} + \hat{w}_i \hat{s}^\dagger) \right] \\ &\quad + [g_{sss} (\hat{s} + \hat{s}^\dagger)^3]. \end{aligned} \quad (1)$$

In this Hamiltonian, the waveguide modes are naturally orthogonal, and each is coupled to the SNAIL with strength $g_{w_i s}$; g_{sss} is the strength of the SNAIL's third-order term. We parametrically drive photon exchange between a pair of waveguide modes by driving the SNAIL at the difference of their frequencies. This scheme has been long used in parametric amplifiers and circulators, where it goes by the name 'noiseless photon conversion'³⁰⁻³². To have independently controllable couplings, we have chosen the SNAIL frequency and waveguide dimensions so that all mode frequencies and frequency differences are unique, with all difference frequencies below the lowest mode frequency (see Supplementary Information³³ section 2, Fig. S2).

As all frequencies are widely separated, we can re-diagonalize the system to eliminate the interaction term, slightly shifting all mode frequencies and definitions (for simplicity's sake we omit any change of variable representation for the new, hybrid eigenmodes), and inducing all possible self- and cross-three-wave couplings among the waveguide modes and SNAIL. This is analogous to common techniques used in circuit QED^{34,35}, with a third-rather than fourth-order nonlinearity. Retaining only the parametric coupling terms we will use in the router,

which is safe as long as all other processes are well separated from any desired process in frequency, we write the effective Hamiltonian of the router as

$$\hat{\mathcal{H}}_R^{\text{eff}}/\hbar = \hat{\mathcal{H}}_{R,0}/\hbar + \sum_{i \neq j} g_{w_i w_j s}^{\text{eff}} (\hat{w}_i^\dagger \hat{w}_j \hat{s} + \hat{w}_i \hat{w}_j^\dagger \hat{s}^\dagger). \quad (2)$$

The effective three-wave interaction strengths are given by, $g_{w_i w_j s}^{\text{eff}} \approx 6g_{sss}(\frac{g}{\Delta})_{w_i s}(\frac{g}{\Delta})_{w_j s}$, where $\Delta_{w_i s} = \omega_{w_i} - \omega_s$. Note, however, that in our experiment we never directly populate these waveguide modes or drive their difference frequencies. Instead these terms serve as a ‘scaffold’ in the router to create similar terms among the module communication modes, as detailed below. The hybridization strengths $(\frac{g}{\Delta})_{w_i s}$ are key parameters as they both limit the eventual parametric coupling strengths and determine how much longer-lived the waveguide modes can be compared to the low-Q SNAIL mode.

Next, we combine our router with the modules’ communication modes. As shown in Fig. 1b, we accomplish this by creating four modules, each containing one mode with a frequency near one of the router’s waveguide modes, and coupled to the router via an aperture in their shared wall. This coupling is again deliberately dispersive, with the strength controlled by a combination of waveguide-communication mode detuning, coupling aperture size, and placement along the router’s length. The router plus communication mode Hamiltonian is written as:

$$\begin{aligned} \hat{\mathcal{H}}_{RC}/\hbar &= \hat{\mathcal{H}}_R/\hbar + \hat{\mathcal{H}}_{C,0}/\hbar + \hat{\mathcal{H}}_{RC,\text{int}}/\hbar \\ &= \hat{\mathcal{H}}_R/\hbar + \left[\sum_i \omega_{c_i} \hat{c}_i^\dagger \hat{c}_i \right] + \left[\sum_i g_{c_i w_i} (\hat{c}_i^\dagger \hat{w}_i + \hat{c}_i \hat{w}_i^\dagger) \right]. \end{aligned} \quad (3)$$

The second and third terms denote the communication mode’s energy and the communication mode-waveguide mode interactions, respectively. As before, we diagonalize this Hamiltonian to eliminate the direct interactions among the modes without changing variable representation, and neglect all but the cavity-cavity third order interactions to find the new effective Hamiltonian for the composite router plus communication modes system:

$$\hat{\mathcal{H}}_{RC}^{\text{eff}}/\hbar = \hat{\mathcal{H}}_{R,0}/\hbar + \hat{\mathcal{H}}_{C,0}/\hbar + \sum_{i \neq j} g_{c_i c_j s}^{\text{eff}} (\hat{c}_i^\dagger \hat{c}_j \hat{s} + \hat{c}_i \hat{c}_j^\dagger \hat{s}^\dagger). \quad (4)$$

The new effective three body interaction strength is $g_{c_i c_j s}^{\text{eff}} \approx g_{w_i w_j s}^{\text{eff}}(\frac{g}{\Delta})_{c_i w_i}(\frac{g}{\Delta})_{c_j w_j}$.

The use of a network of hybridization, linking the cavity modes to the central SNAIL via intermediate cavity modes comes with advantages: choosing each dispersive coupling $g/\Delta \simeq 0.1$ the communication modes can live up to 10^4 times longer than the SNAIL mode and 100 times longer than the waveguide modes, greatly decreasing the need for long lifetime components in the router. More, the dispersive couplings and parametric

driving are insensitive to modest errors in mode frequencies, again reducing the need for precision fabrication, unlike photon exchange techniques based on resonant mode couplings^{21,36}. It is certainly possible to remove the intermediate waveguide modes in a monolithic version of our design, though this comes with both greatly reduced flexibility in combining disparate elements and more stringent requirements for the SNAIL’s lifetime.

In operation, the parametrically driven two-body exchange rate, for example between modes C_i and C_j , is $\sqrt{n_s} g_{c_i c_j s}^{\text{eff}}$, where n_s is the pump strength expressed as a photon number (see SI section II.A). It is here that we find the price for our hybridization network: the effective three body coupling has been greatly reduced ($g_{c_i c_j s}^{\text{eff}} \simeq 6 \times 10^{-4} g_{sss}$). To achieve rapid gates with feasible pump strengths, we must both engineer g_{sss} to be large and carefully design the pump line (and the SNAIL itself) to tolerate very strong drives to compensate this dilution of nonlinearity.

It is also important to note that Eq. 4 represents only our desired coupling terms, in practice all modes inherit both self- and cross- three-wave mixing terms from the SNAIL. Of particular concern are couplings between a cavity and non-adjacent waveguide modes (ex. C_3 to W_4), in practice we choose a minimum waveguide to cavity spacing of ~ 100 MHz to suppress cross-talk with these couplings. This difference frequency is comparable to the anharmonicity of transmon qubits; similarly, we can use variants of the DRAG³⁷ technique to drive rapid swap gates among the communication modes without leakage to unwanted modes (see SI section IV).

III. RESULTS

Basic router characterization with coherent states. For initial experiments, we connected our router to four simple modules (see SI sections I and Methods for details), but omitted the module qubits. Each communication mode is driven and read out via a ‘weak’ port whose induced relaxation rate is much smaller than the mode’s internal loss rate. Figure 2a shows an experimental pulse sequence for swapping coherent states between the module communication modes C_2 and C_4 . First, a short on-resonance drive is applied to C_4 through the weakly coupled port, which creates a coherent state in this cavity. Then, a pump tone is applied to the SNAIL mode near the $C_2 - C_4$ difference frequency: $\omega_p = \omega_{c_4} - \omega_{c_2} + \delta$, where δ is the pump detuning relative to the measured frequency difference between two cavity mode. Meanwhile, the light in these two cavities are monitored by receiving the I-Q voltage leaking out from each cavity’s weakly coupled port. By varying the applied pump frequency and time, we can determine both the swap rate and resonant condition for pumping.

The experiment results are shown in Fig. 2b, c. There is good agreement between the envelope of the swap trace (green and purple lines) and the hybridized decay trace,

indicating that the state is only swapping between these two cavities without leaking into other modes, and that the SWAP gate fidelity is mainly limited by the lifetime of these two cavities. The same experiment was performed for all the six possible pairs of the four communication modes, the fastest full-swap time was 375 ns, and the slowest was 1248 ns, with an average swap time of ~ 760 ns (see SI sections II.B and Table S2). On average, the pump frequency required to fully swap light between the two cavities was detuned by several hundred kHz (-416 kHz for the data in Figure 2). We attribute this to a combination of SNAIL- and communication-mode static and dynamic Kerr effects. This has strong parallels to saturation effects in parametric amplifiers^{29,38–40}, though here the primary consequence is just that we must track these shifts in our control electronics.

Operation as a modular quantum computer with single-qubit modules. Next, we added the transmon qubits to complete modules 2-4 (Module one's qubit was omitted), and operated the full device as a small, modular, quantum computer. Each single-qubit-module consists of one communication cavity C_i , one transmon Q_i and one readout cavity R_i . The machine's layout is shown schematically in Fig. 1c. For simplicity, our qubit states throughout the system are the Fock states $|0\rangle$ and $|1\rangle$, although the communication modes could in principle support a variety of more complex encodings. We create intra-module gates between each qubit and its communication cavity using established four-wave-mixing Hamiltonian and doubly pumped parametric transitions (see^{13,18,23} and SI section III for details). Unlike our inter-module SWAPs, the intra-module SWAPs are based on cross-Kerr couplings between qubit and cavity, and as such require paired drives on both qubit and cavity (as indicated in Fig. 3b) to operate.

We next use the module transmons and intra-module SWAP operations to swap Fock states across the router, transferring single photons between distant qubits as shown in Fig. 3a, b. The protocol begins with all qubits and cavities prepared in their ground states. A $R_x(\pi)$ pulse is first applied to Q_2 and brings it to the excited state. Next, an intra-module SWAP gate is performed between Q_2 and C_2 . This fully swaps the excitation from Q_2 to C_2 . Third, the photon is swapped between C_2 and C_4 across the router by pumping on the SNAIL mode, just as demonstrated in Figure 2. The SNAIL pump duration is varied, which will result in an effective Rabi oscillation between the two qubits when the protocol is completed. Finally, we apply two more intra-module SWAP gates, C_2 to Q_2 and C_4 to Q_4 , which fully transfer the states of C_2 and C_4 to their module qubits, which are then measured simultaneously using dispersive readout of the readout (R) modes. The results are shown in Fig. 3c and 3d. The transfer fidelity between Q_4 and Q_2 is $72.5 \pm 1.17\%$. We perform Lindblad master equation simulations assuming ideal interactions, with the only defects being all modes' measured coherences (see Methods); the simulation results (dotted

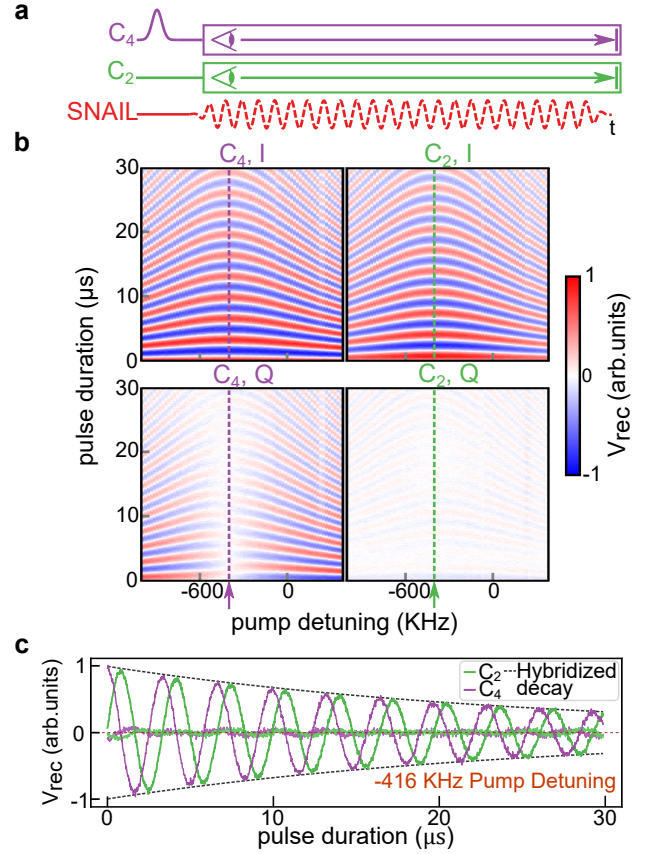


Figure 2. Coherent state exchange between communication cavities (a) Pulse sequence of the swap experiment. We begin by displacing one cavity to create a coherent state, which we then swap between a pair of cavities by applying a parametric drive to the SNAIL. We continuously monitor the I-Q voltage in each cavity during the swap process. (b) In- and quadrature-phase received voltage from the two cavities versus pulse duration and pump detuning from the nominal difference frequency. The dashed vertical line denotes the optimal detuning frequency for full photon exchange. (c) Linecut of (b) at the optimal full-swap detuning. The grey dashed envelope represents the theoretical hybridized decay trace of C_2 and C_4 , given by $\exp[-2t(1/\tau_2 + 1/\tau_4)]$, where τ_2 and τ_4 are the decoherence times of C_2 and C_4 , respectively.

curves) show good quantitative agreement with our data, indicating that, as with coherent state operation, the primary fidelity limit in our system is the ratio of gate time to our modes' coherence times. The uncertainty given for the Fock state transfer fidelity, and all following quoted fidelities, is calculated following the 'bootstrap method' in^{41,42}. No correction is applied for State Preparation and Measurement (SPAM) errors. Details of our data processing and experimentally determined SPAM errors can be found in SI section I.

Inter-module Bell state generation. To this point, we have employed the router only to fully swap states between pairs of communication modes, relying on the fact that our exchange interaction will swap coherent states and Fock states fully from one cavity to the other. How-

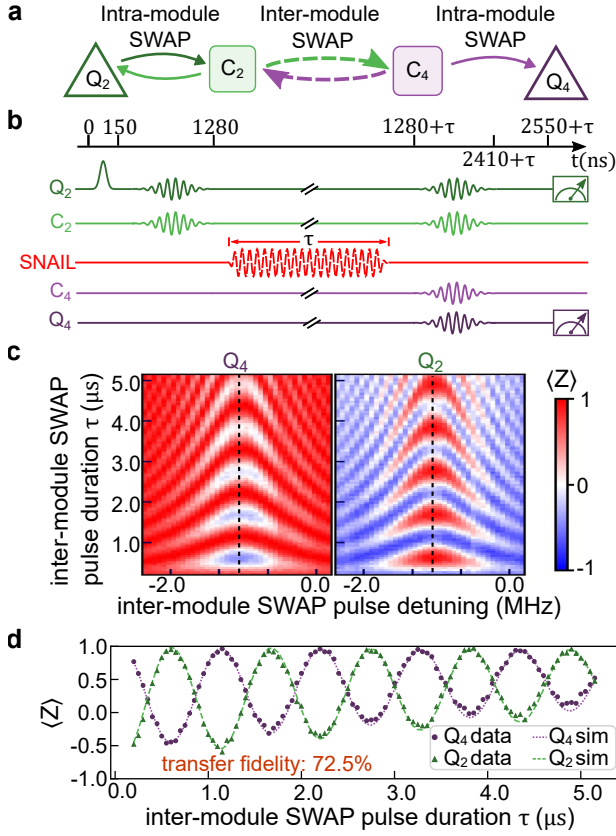


Figure 3. Fock state swap experiment between remote qubits. (a) Illustration of the photon swap protocol, in which a photon, originating in Q_2 is fully swapped to C_2 , and then, depending on the variable inter-module pulse duration, routed to Q_4 or returned to Q_2 . (b) Experiment pulse sequence. A photon is created in Q_2 , then swapped to C_2 . Next it is swapped (or not) to C_4 with a variable duration inter-module SWAP pulse, and finally the light in $C_{2,4}$ are routed via further intra-module SWAPs to their respective qubits, which are then measured. The upper black bar indicates the total experimental duration with τ describing the variable, SNAIL actuated inter-module SWAP. (c) Measurement result of Q_2 and Q_4 for different SNAIL pump detuning and duration. Here the color of 2D sweep indicates the measurement along qubits' z -axis. (d) A cut of the swap data along the dotted line indicated in (c). The green triangles and purple circles are Q_2 and Q_4 data, respectively, and the dashed lines are the corresponding simulation results.

ever, this analogy breaks down for both our intra- and inter-module swaps between a qubit and cavity and a pair of cavities, when we consider arbitrary pulse lengths and certain joint qubit-cavity states (ex. $|1, 1\rangle$). For this reason some researchers choose to refer to these gates between pairs of cavities as ‘beam splitters’^{23,43} for their obvious resemblance to the optical component of the same name. This analogy, however, fails for our qubit-cavity interactions, and so we choose instead to refer to these gates via the exponent which determines their unitary relative to a full SWAP gate, i.e. a $\sqrt{\text{SWAP}}$ is de-

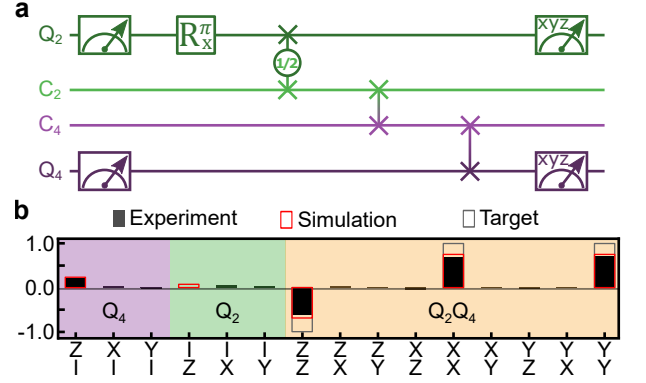


Figure 4. Inter-module Bell state generation. (a) Quantum circuit for generating a Bell state between Q_2 and Q_4 . Entanglement is first generated between Q_2 and C_2 using a $\sqrt{\text{SWAP}}$ gate, the cavity component is then moved to Q_4 using two full-SWAP gates. (b) Tomography of the joint Q_2, Q_4 Bloch vector, in which each bar represent a joint measurement of the two qubits in the basis indicated (I indicates no measurement). Here the black bars indicate the experiment result, the red rectangles are master-equation simulation results, while the gray rectangles are the target pure Bell state. The fidelity to target Bell state $\frac{1}{\sqrt{2}}(|01\rangle + |10\rangle)$ is $76.9 \pm 0.76\%$, which agrees very well with the simulation prediction of 77.2% .

scribed by $U_{\text{SWAP}}^{\frac{1}{2}}$. As we only swap light into empty qubits/cavities in our protocols, and so never occupy states containing two or more photons, this inexact analogy will yield both a simple graphical and conceptual picture of our gates as well as correct intuition about the system’s evolution during our protocols. This issue, however, must obviously be revisited for alternate qubit encoding choices.

Next, we use such a gate, a $\sqrt{\text{SWAP}}$, created by shortening the first intra-module SWAP gate from Figure 3 by close to $1/2$ in duration to create inter-module Bell states. The $\sqrt{\text{SWAP}}$ has the effect of taking the single photon in the qubit and coherently ‘sharing’ it between the qubit and cavity, creating a Bell state between the two modes. Overall, the sequence first creates a Bell-pair inside a module, and then shifts the communication cavity’s component to a qubit in a second module. The quantum circuit is shown in Fig. 4a. Tomography is performed on both qubits, while the communication cavities are not measured. The measurement results are shown in Fig. 4b. From this tomographic data we can reconstruct the density matrix of the Q_2 and Q_4 . We achieve a Bell fidelity of $76.9 \pm 0.76\%$. The same experiments were performed on the other two qubit pairs $Q_2 - Q_3$ and $Q_4 - Q_3$ with fidelity of $58.7 \pm 2.40\%$ and $68.2 \pm 0.83\%$, respectively. The results were again compared with Lindblad master equation simulations (red rectangles in Fig. 4b), and show that the dominant source of infidelity remains the modes’ lifetimes.

Parallel operations Another advantage of our archi-

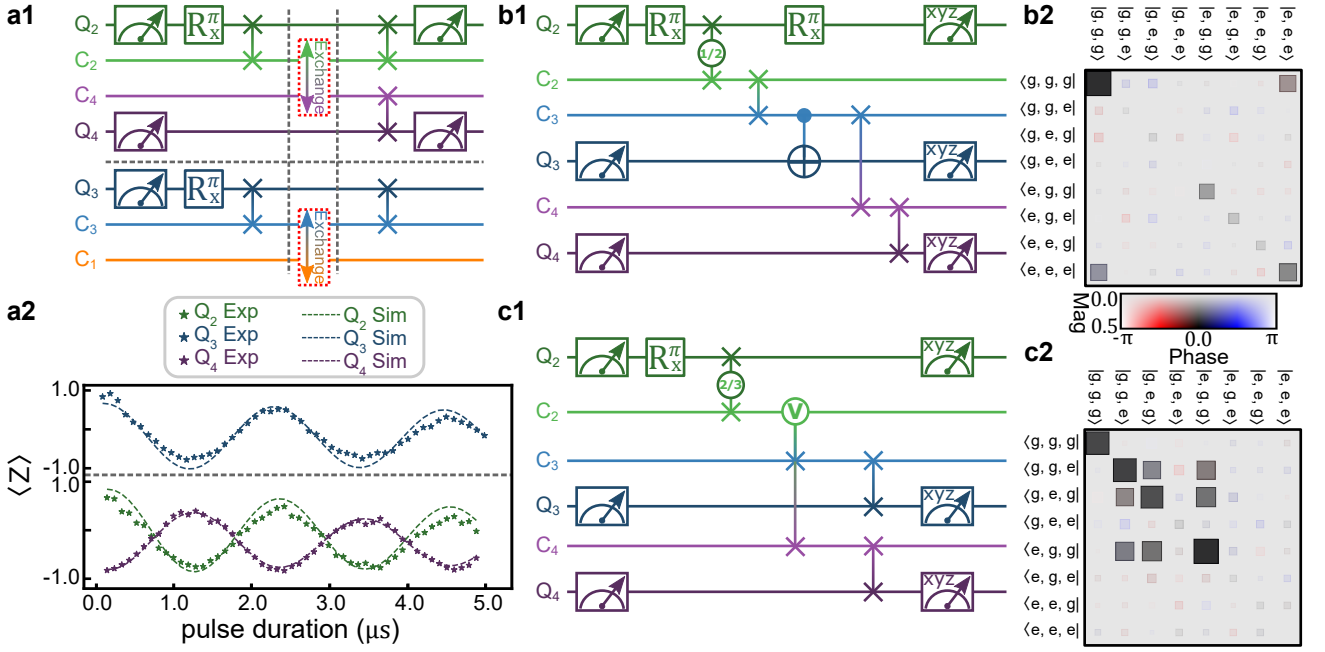


Figure 5. **Parallel SWAP, and GHZ and W state generation experiments.** (a1) Gate sequence for parallel photon exchange over the router. (a2) Photon population of all three qubits vs. router swap time. The dots here are the experimental results, and the corresponding dashed lines are simulation results. (b1) GHZ state generation sequence. (b2) GHZ state generation density matrix reconstructed from tomography. Here the size of each block represents the magnitude of each element in density matrix, and the 2-D color scale represents each element's phase as a function of both color and magnitude, with bright colors for large elements fading to neutral gray for small magnitudes to avoid drawing the eye to small, noisy matrix elements. The observed fidelity state is $48.9 \pm 5.27\%$ (c1) W state generation pulse sequence. Together, the $\text{SWAP}^{2 \arctan(\sqrt{2})/\pi}$ and 'V-SWAP' gates create a W state distributed across Q₂, C₃, and C₄. The subsequent SWAPs redirect the latter two components to Q₃ and Q₄, respectively. (c2) Hinton diagram of results of W-state generation sequence; the observed fidelity state is $53.4 \pm 2.56\%$.

ture is that we can drive multiple parametric operations in the router simultaneously, which enables parallel operation and new ways to create entanglement. We have demonstrated the simplest implementation of parallel operations by swapping light between two pairs of modules simultaneously. Here, M₂ and M₄ are treated as one sub-system, while M₃ and M₁ form a second. We swap a photon from Q₂ to Q₄ and Q₃ to C₁ across the router simultaneously. The gate sequence is shown in Fig. 5a1. The two cross module swap interactions, C₂ – C₄ and C₃ – C₀, are turned on simultaneously by pumping the SNAIL mode at the two frequency differences using a room-temperature combiner. The SNAIL pumps are applied for a variable period. The protocol concludes with SWAP gates between all cavity-qubit pairs and measurement of all qubits. The results (Fig. 5a2) show that Fock states can swap between both pairs of modules simultaneously without interference or enhanced relaxation, as shown by comparison to master equation simulations. The drive frequencies for parallel swap processes in the router needs frequency adjustments on order ~ 100 kHz compared to the single SWAP case, which we attribute to dynamic and static cross-Kerr effects due to the paired SNAIL drives. We reduced the pump strengths, slowing the gates from 600 ns to 1300 ns as we saw excess deco-

herence when running two parallel processes at maximum pump strength. We do not believe this is a fundamental limitation, but can be improved in future experiment by optimized SNAIL and router design.

As further proof of the quantum coherence of parallel operations in the router, we also repeated the Bell state generation protocol between Q₂ and Q₄ with the M₁ – M₃ SWAP activated in parallel. Again, the pump strengths were decreased, slowing the inter-module SWAP time. We achieved a Bell state fidelity of $68.1 \pm 0.79\%$, while the simulated fidelity is 68.4 %). Here the decrease of fidelity compared to the single Bell state generation process (which has a fidelity of $76.9 \pm 0.76\%$) is due to the longer gate time used for the C₂ – C₄ SWAP in the presence of a parallel SWAP operation.

Full-router sequences To this point, we have listed only state fidelities, which are limited both by the mode lifetimes in our system, as well as the number of gates required to perform both intra- and inter-module operations in the same pulse sequence. We can estimate the performance of the router itself by estimating the 'average' fidelity of the inter-module gates. Given the average gate time of $T_{gate,avg} \simeq 760$ ns, and the average decoherence time of our communication modes of $T_{C,avg} \simeq 22$ μ s we find $F_{avg} = 1 - \frac{T_{gate,avg}}{T_{C,avg}} = 0.97$. Even given this

performance, extending to still longer sequences which can entangle all qubits in the system is very challenging due to the further decay caused by increased gate count and the delicacy of larger entangled states. Nevertheless, we implemented two further router-wide sequences to demonstrate further capabilities of our system.

First, we explored the use of two simultaneous swap processes which link one ‘source’ cavity to two ‘target’ cavities, which we refer to as a ‘V-SWAP’. As shown in SI section II.C, this form of SWAP for a certain duration empties the source cavity, coherently and symmetrically swapping its contents into the target cavities. By combining the V-SWAP with a $\text{SWAP}^{2\arctan(\sqrt{2})/\pi}$ (which leaves $1/3$ photon in the source mode) as shown in Fig. 5c1, we can take a single photon from Q_2 and use our inter-module V-swap to create a W-state shared among all three modules. We achieve a fidelity for this state of $53.4 \pm 2.56\%$ (see state reconstruction in Fig. 5c2).

We also sought to create a GHZ state shared among all three modules’ qubits. As we implement it in Fig. 5b1, this protocol require one additional entangling gate: an intra-module CNOT. We achieve this using a state selective qubit π -pulse⁴⁴. We reconstruct the final state from tomography as shown in Fig. 5b2, and find a fidelity of $48.9 \pm 5.27\%$, just below the threshold for provable entanglement. While both results follow below the threshold for provable entanglement, they point to our ability to implement an extensive gate set in the router.

DISCUSSION AND OUTLOOK

In this work we have demonstrated a coherent quantum state router for microwave photons and used it to realize a small modular quantum computer. A key feature is the use of a SNAIL mode to create three-wave couplings in the router itself, rather than rely on nonlinear couplers embedded in each module. The router enables us to create all-to-all couplings among a set of quantum modules, to parametrically drive gates between the communication modes of those modules, and even create three-qubit and parallel SWAP operations between multiple pairs of communication modes by applying multiple, simultaneous parametric drives.

The current device’s performance ($F_{avg} = 0.97$ for gates involving the router) is limited primarily by the qubit/cavity lifetimes involved, though the limitation is primarily in the modules themselves and due to imperfect quantum engineering. Other recent implementations of similar quantum modules^{18,23} have achieved much higher coherence time, with qubit and cavity modes in the $100 - 1000\mu\text{s}$ range. With modest improvements in lifetime to $\sim 10\mu\text{s}$ for our router waveguide modes, which we can achieve by retracting our SNAIL into a coupling tube⁴⁵, our router will be able to provide sub-microsecond, very high fidelity gates between millisecond scale communication cavities. Retracting the SNAIL into a tube adjacent to the waveguide also has the advantage

that we can couple a single SNAIL to multiple router elements, allowing us create inter-router operations and hence a scalable modular network.

One vital question requiring further research is how fast we can ultimately drive gates in this system. One straightforward route is to further increase the waveguide mode lifetimes in the router; we can then increase the dispersive coupling strength to their respective communication modes without decreasing the communication mode lifetimes. Doubling our current average coupling to $g/\Delta = 0.2$ will immediately push our average gate time to ~ 100 ns. We must also learn more about how hard we can drive SNAILs with one or more drive tones. This is directly related to the issue of saturation power in parametric amplifiers, where recent exciting results^{29,46} provide guidance on how we may further optimize our router. Coupled with stronger module-router couplings, it seems feasible to push our overall gate time down to as low as tens of nanoseconds in better optimized, next generation devices.

REFERENCES

- ¹Cirac, J. I., Zoller, P., Kimble, H. J. & Mabuchi, H. Quantum State Transfer and Entanglement Distribution among Distant Nodes in a Quantum Network. *Phys. Rev. Lett.* **78**, 3221–3224 (1997). URL <https://link.aps.org/doi/10.1103/PhysRevLett.78.3221>. Publisher: American Physical Society.
- ²Kimble, H. J. The quantum internet. *Nature* **453**, 1023–1030 (2008). URL <https://www.nature.com/articles/nature07127>. Number: 7198 Publisher: Nature Publishing Group.
- ³Monroe, C. & Kim, J. Scaling the ion trap quantum processor. *Science* **339**, 1164–1169 (2013).
- ⁴Monroe, C. R., Schoelkopf, R. J. & Lukin, M. D. Quantum connections. *Scientific American* **314**, 50–57 (2016).
- ⁵Chou, C.-W. *et al.* Measurement-induced entanglement for excitation stored in remote atomic ensembles. *Nature* **438**, 828–832 (2005).
- ⁶Moehring, D. L. *et al.* Entanglement of single-atom quantum bits at a distance. *Nature* **449**, 68–71 (2007).
- ⁷Ritter, S. *et al.* An elementary quantum network of single atoms in optical cavities. *Nature* **484**, 195–200 (2012).
- ⁸Hofmann, J. *et al.* Heralded entanglement between widely separated atoms. *Science* **337**, 72–75 (2012).
- ⁹Bernien, H. *et al.* Heralded entanglement between solid-state qubits separated by three metres. *Nature* **497**, 86–90 (2013).
- ¹⁰Wengerowsky, S. *et al.* Entanglement distribution over a 96-km-long submarine optical fiber. *Proceedings of the National Academy of Sciences* **116**, 6684–6688 (2019).
- ¹¹Yu, Y. *et al.* Entanglement of two quantum memories via fibres over dozens of kilometres. *Nature* **578**, 240–245 (2020).
- ¹²Roch, N. *et al.* Observation of measurement-induced entanglement and quantum trajectories of remote superconducting qubits. *Physical review letters* **112**, 170501 (2014).
- ¹³Narla, A. *et al.* Robust concurrent remote entanglement between two superconducting qubits. *Physical Review X* **6**, 031036 (2016).
- ¹⁴Dickel, C. *et al.* Chip-to-chip entanglement of transmon qubits using engineered measurement fields. *Physical Review B* **97**, 064508 (2018).
- ¹⁵Kurpiers, P. *et al.* Quantum communication with time-bin encoded microwave photons. *Physical Review Applied* **12**, 044067 (2019).
- ¹⁶Monroe, C. *et al.* Large-scale modular quantum-computer archi-

- ture with atomic memory and photonic interconnects. *Phys. Rev. A* **89**, 022317 (2014). URL <https://link.aps.org/doi/10.1103/PhysRevA.89.022317>. Publisher: American Physical Society.
- ¹⁷Linke, N. M. *et al.* Experimental comparison of two quantum computing architectures. *PNAS* **114**, 3305–3310 (2017). URL <https://www.pnas.org/content/114/13/3305>. Publisher: National Academy of Sciences Section: Physical Sciences.
- ¹⁸Axline, C. J. *et al.* On-demand quantum state transfer and entanglement between remote microwave cavity memories. *Nature Physics* **14**, 705–710 (2018).
- ¹⁹Campagne-Ibarcq, P. *et al.* Deterministic remote entanglement of superconducting circuits through microwave two-photon transitions. *Phys. Rev. Lett.* **120**, 200501 (2018). URL <https://link.aps.org/doi/10.1103/PhysRevLett.120.200501>.
- ²⁰Kurpiers, P. *et al.* Deterministic quantum state transfer and remote entanglement using microwave photons. *Nature* **558**, 264–267 (2018).
- ²¹Leung, N. *et al.* Deterministic bidirectional communication and remote entanglement generation between superconducting qubits. *npj Quantum Inf* **5**, 1–5 (2019). URL <https://www.nature.com/articles/s41534-019-0128-0>.
- ²²Magnard, P. *et al.* Microwave quantum link between superconducting circuits housed in spatially separated cryogenic systems. *Physical Review Letters* **125**, 260502 (2020).
- ²³Burkhart, L. D. *et al.* Error-detected state transfer and entanglement in a superconducting quantum network. *PRX Quantum* **2**, 030321 (2021).
- ²⁴Zhong, Y. *et al.* Deterministic multi-qubit entanglement in a quantum network. *Nature* **590**, 571–575 (2021). URL <https://www.nature.com/articles/s41586-021-03288-7>. Number: 7847 Publisher: Nature Publishing Group.
- ²⁵Frattini, N. *et al.* 3-wave mixing Josephson dipole element. *Applied Physics Letters* **110**, 222603 (2017).
- ²⁶Vlastakis, B. *et al.* Deterministically Encoding Quantum Information Using 100-Photon Schrödinger Cat States. *Science* **342**, 607–610 (2013). URL <https://science.sciencemag.org/content/342/6158/607>. Publisher: American Association for the Advancement of Science Section: Report.
- ²⁷Michael, M. H. *et al.* New Class of Quantum Error-Correcting Codes for a Bosonic Mode. *Phys. Rev. X* **6**, 031006 (2016). URL <https://link.aps.org/doi/10.1103/PhysRevX.6.031006>. Publisher: American Physical Society.
- ²⁸Gottesman, D., Kitaev, A. & Preskill, J. Encoding a qubit in an oscillator. *Phys. Rev. A* **64**, 012310 (2001). URL <https://link.aps.org/doi/10.1103/PhysRevA.64.012310>. Publisher: American Physical Society.
- ²⁹Sivak, V. *et al.* Kerr-Free Three-Wave Mixing in Superconducting Quantum Circuits. *Phys. Rev. Applied* **11**, 054060 (2019). URL <https://link.aps.org/doi/10.1103/PhysRevApplied.11.054060>. Publisher: American Physical Society.
- ³⁰Bergeal, N. *et al.* Analog information processing at the quantum limit with a Josephson ring modulator. *Nature Physics* **6**, 296–302 (2010). URL <https://www.nature.com/articles/nphys1516>.
- ³¹Sliwa, K. M. *et al.* Reconfigurable Josephson Circulator/Directional Amplifier. *Phys. Rev. X* **5**, 041020 (2015). URL <https://link.aps.org/doi/10.1103/PhysRevX.5.041020>. Publisher: American Physical Society.
- ³²Lecocq, F. *et al.* Nonreciprocal microwave signal processing with a field-programmable Josephson amplifier. *Physical Review Applied* **7**, 024028 (2017).
- ³³See supplementary information available at xxx for details.
- ³⁴Nigg, S. E. *et al.* Black-Box Superconducting Circuit Quantization. *Phys. Rev. Lett.* **108**, 240502 (2012). URL <https://link.aps.org/doi/10.1103/PhysRevLett.108.240502>. Publisher: American Physical Society.
- ³⁵Mineev, Z. K. *et al.* Energy-participation quantization of Josephson circuits. *npj Quantum Information* **7**, 1–11 (2021).
- ³⁶Bialczak, R. C. *et al.* Fast Tunable Coupler for Superconducting Qubits. *Phys. Rev. Lett.* **106**, 060501 (2011). URL <https://link.aps.org/doi/10.1103/PhysRevLett.106.060501>. Publisher: American Physical Society.
- ³⁷Motzoi, F., Gambetta, J. M., Reberntrost, P. & Wilhelm, F. K. Simple Pulses for Elimination of Leakage in Weakly Nonlinear Qubits. *Physical Review Letters* **103**, 110501 (2009). URL <https://link.aps.org/doi/10.1103/PhysRevLett.103.110501>.
- ³⁸Frattini, N., Sivak, V., Lingenfelter, A., Shankar, S. & Devoret, M. Optimizing the nonlinearity and dissipation of a SNAIL parametric amplifier for dynamic range. *Physical Review Applied* **10**, 054020 (2018).
- ³⁹Planat, L. *et al.* Understanding the Saturation Power of Josephson Parametric Amplifiers Made from SQUID Arrays. *Phys. Rev. Applied* **11**, 034014 (2019). URL <https://link.aps.org/doi/10.1103/PhysRevApplied.11.034014>.
- ⁴⁰Liu, C., Chien, T.-C., Hatridge, M. & Pekker, D. Optimizing Josephson-ring-modulator-based Josephson parametric amplifiers via full Hamiltonian control. *Phys. Rev. A* **101**, 042323 (2020). URL <https://link.aps.org/doi/10.1103/PhysRevA.101.042323>.
- ⁴¹Newman, M. E. J. & Barkema, G. T. *Monte Carlo Methods in Statistical Physics* (Clarendon Press, 1999). Google-Books-ID: KKL2nQEACAAJ.
- ⁴²Young, P. *Everything you wanted to know about data analysis and fitting but were afraid to ask* (Springer, 2015).
- ⁴³Pfaff, W. *et al.* Controlled release of multiphoton quantum states from a microwave cavity memory. *Nature Physics* **13**, 882–887 (2017).
- ⁴⁴Schuster, D. *et al.* Resolving photon number states in a superconducting circuit. *Nature* **445**, 515–518 (2007).
- ⁴⁵Axline, C. J. *Building blocks for modular circuit QED quantum computing*. Ph.D. thesis, Yale University (2018).
- ⁴⁶Parker, D. J. *et al.* A near-ideal degenerate parametric amplifier. *arXiv preprint arXiv:2108.10471* (2021).
- ⁴⁷Place, A. P. *et al.* New material platform for superconducting transmon qubits with coherence times exceeding 0.3 milliseconds. *Nature communications* **12**, 1–6 (2021).
- ⁴⁸Breuer, H.-P., Petruccione, F. *et al.* *The theory of open quantum systems* (Oxford University Press on Demand, 2002).
- ⁴⁹Johansson, J. R., Nation, P. D. & Nori, F. QuTiP 2: A Python framework for the dynamics of open quantum systems. *Computer Physics Communications* **184**, 1234–1240 (2013). URL <https://www.sciencedirect.com/science/article/pii/S0010465512003955>.

METHODS

Device fabrication The device in Fig. 1d contains a SNAIL on a sapphire chip, three transmon qubits on individual sapphire chips, and multiple 3D resonator modes coupled with each other as shown in Fig. 1c. The coupling between the SNAIL and waveguide modes is determined by the shape of the SNAIL antenna (Extended Data Fig. 2b), which is fabricated using photolithography and acid etching from a 200-nm thin tantalum film on a c-plane sapphire substrate⁴⁷. Two windows were opened on the 3D waveguide above and below the SNAIL chip to place a copper magnet and a pump port into the waveguide close to the SNAIL to enable flux bias and strong pumping (Extended Data Fig. 2a). The antennae of the transmon qubits are fabricated using the same tantalum etching technique, while both the SNAIL and transmon junctions are made of Al-AlO_x-Al layers fabricated using a standard Dolan bridge method.

SNAIL mode characterization. The SNAIL mode

is characterized by measuring the transmission signal from the SNAIL pump port to a side port on the waveguide using a network analyzer. By sweeping the bias current applied to the magnet (Extended Data Fig. 2c) we can measure how the frequency of the SNAIL and waveguide modes are changed by flux biasing the SNAIL loop.

Experimental setup. The modular quantum computer is installed at the base (~ 18 mK) plate of a cryogenic set-up (Extended Data Figure 1). Here, all pulse sequences are generated by Keysight M3202A (1 GSa/s) and M3201A (500 MSa/s) Arbitrary Waveform Generators (AWGs). The baseband microwave control pulses are generated at an intermediate frequency (IF) of 100 MHz and upconverted to microwave frequencies

using IQ mixers. Image rejection (IR) mixers have been used for downconverting the detected signals to 50 MHz, which are then digitized using a control system based on Keysight M3102A Analog-to-Digital converters with a sampling rate of 500 MSa/s and on-board Field-Programmable Gate Arrays (FPGA) for signal processing.

Numerical simulations. We simulate the behavior of our system by analyzing the behavior of seven modes participating in the experiments: three qubit modes and four communication modes. We treat the gates as ideal parametric interactions, and work in the rotating frame of the system (details in SI section II.A). The Hamiltonian, then, contains single qubit controls, cavity-cavity inter-module interactions, and qubit-cavity intra-module interactions listed respectively to give:

$$\hat{H}_{QC}/\hbar = \sum_{m=2,3,4} \eta_m (\hat{q}_m^\dagger + \hat{q}_m) + \sum_{\substack{i,j=1,2,3,4 \\ i \neq j}} \eta_{ij} g_{c_i c_j s} (\hat{c}_i^\dagger \hat{c}_j + \hat{c}_i \hat{c}_j^\dagger) + \sum_{k=2,3,4} \eta_k g_{q_k c_k c_k} (\hat{c}_k^\dagger \hat{q}_k + \hat{c}_k \hat{q}_k^\dagger), \quad (5)$$

where \hat{q}_i indicates the qubit mode in each module and $\eta(t)$ represents the time-dependent strength of a given pulse, which follows the shapes and durations used in the experiment. To capture the effects of photon loss and decoherence in the system, we add loss operators with rates corresponding to the measured values listed in SI Table 1 and simulate the evolution of the system via Lindblad master equation⁴⁸ using QuTiP⁴⁹:

$$\dot{\rho}(t) = -\frac{i}{\hbar} [\hat{H}_{QC}(t), \rho(t)] + \sum_n \mathcal{D}[\hat{C}_n](\rho) \quad (6)$$

where ρ represents the density matrix of the system and $\mathcal{D}[\hat{C}_n](\rho) = \hat{C}_n \rho \hat{C}_n^\dagger - 1/2 (\hat{C}_n^\dagger \hat{C}_n \rho + \rho \hat{C}_n^\dagger \hat{C}_n)$ is the interaction between the system and the environment for different collapse operators.

For all experiments reported in the main text, we have applied same pulse sequences in the simulation, and record the final states after half of the measurement time (to account for decay during the measurement process). Results are very consistent between experiments and simulation, which indicates that our device is primarily limited by the coherence times of our modes.

Data processing. For all quoted fidelities in the main text, we have first reconstructed the density matrix ρ from tomographic measurements, and for a given target state σ , the fidelity of the results is calculated using:

$$F(\rho, \sigma) = \left(\text{tr} \sqrt{\sqrt{\rho} \sigma \sqrt{\rho}} \right)^2 \quad (7)$$

Furthermore, a bootstrap method⁴² has been used to

estimate the uncertainty of the reported fidelity. In experiments, all final datasets contain more than 10,000 averages; we restructure the data set into $N_{\text{boot}} = 1,000$ data sets each containing $N = 10,000$ points obtained by Monte Carlo sampling of the original set of 10,000 points. During Monte Carlo sampling, the probability that a data point is picked is $1/N$ irrespective of whether it has been picked before. In the end, we calculate the standard deviation of the bootstrap data sets s_{x^B} .

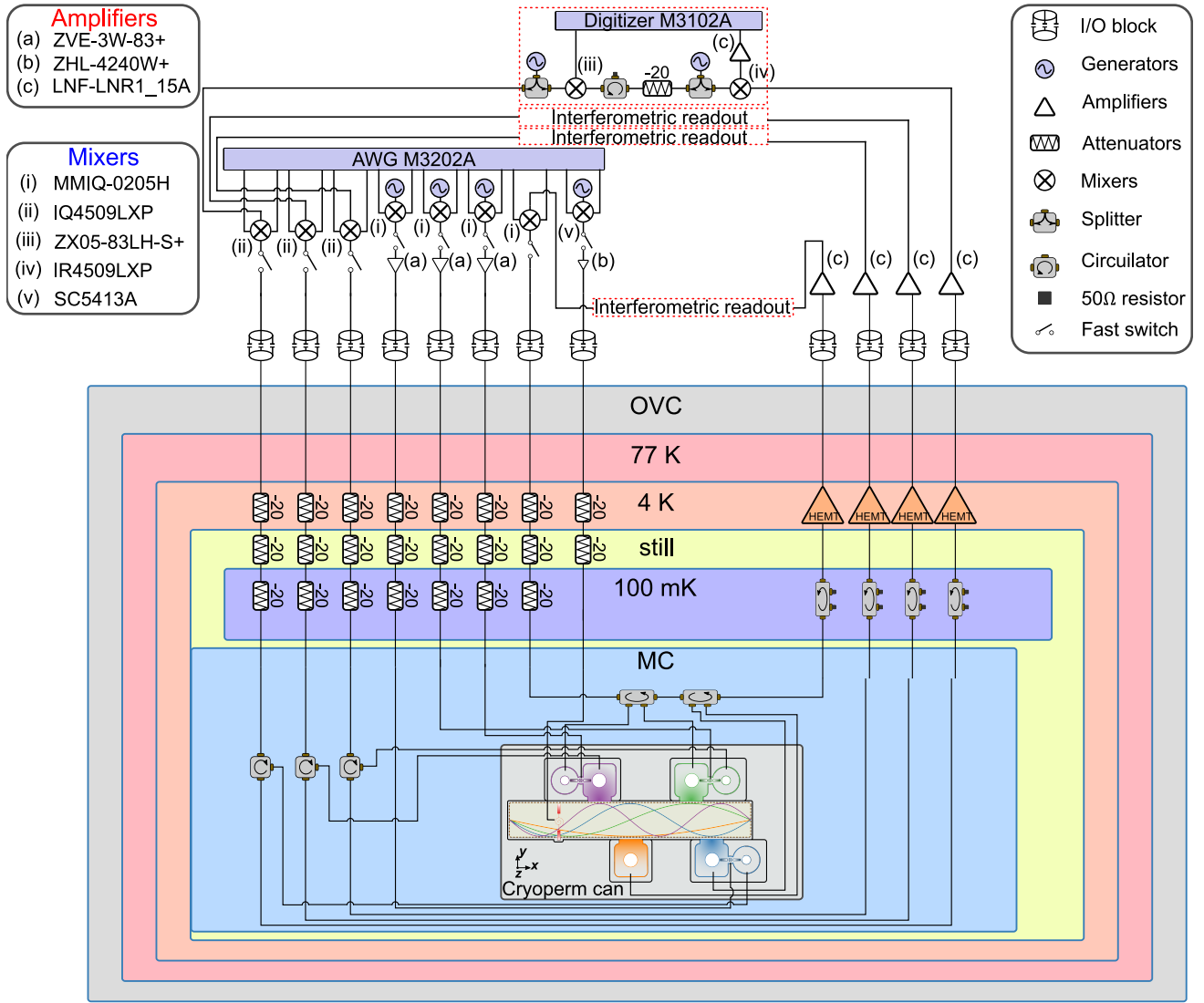
In general, s_{x^B} should have the relation with the uncertainty of the original sample σ_x as:

$$\sigma_x = \sqrt{\frac{N}{N-1}} s_{x^B} \quad (8)$$

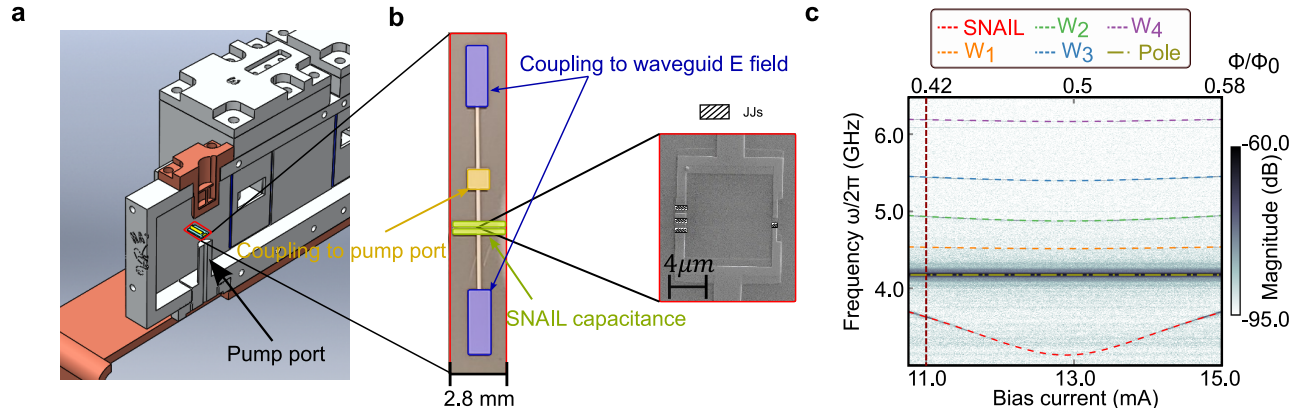
Since, in our case, $N = 10,000$ is sufficiently large, the square root can be replaced by unity.

ACKNOWLEDGEMENTS

The authors gratefully acknowledge the skilled machining and advice of William Strang, and Shyam Shankar, Kevin Chou, Konrad Lehnert, and Robert Schoelkopf for fruitful discussions. We also wish to acknowledge Alex Place and Andrew Houck for help in developing tantalum-based transmon and SNAIL fabrication. This material is based upon work supported by the Air Force Office of Scientific Research under award number FA9550-15-1-0015. This work was also partially supported by the Charles E. Kaufman Foundation of the Pittsburgh Foundation, as well as the Army Research Office under contracts W911NF-18-1-0144 and W911NF-15-1-0397.



Extended Data Figure 1. **Schematic of the experimental setup**



Extended Data Figure 2. **SNAIL mode details.**(a) Physical position of the SNAIL chip and pumping port. The SNAIL is flux-biased via a copper-sheathed electromagnet protruding into the waveguide above it, and is strongly coupled to a microwave drive line introduced via an aluminum cylinder below the SNAIL. (b) False color optical and SEM image of the SNAIL, indicating its essential components. (c) Color plot of the magnitude of transmission signal versus the frequency from SNAIL pumping port ($|S_{21}(\omega)|$) for a range of applied coil bias current/applied SNAIL flux. The dotted lines indicate the dressed modes of the waveguide modes and snail, as well as the ‘pole mode’ of the aluminum cylinder containing the drive port. The vertical dark red dash line indicates the operating flux of the SNAIL.